ADVANCED MATERIALS INTERFACES
www.advmatinterfaces.de

Cathodoluminescence Spectroscopy of Complex Dendritic Au Architectures for Application in Plasmon-Mediated Photocatalysis and as SERS Substrates

Zelio Fusco, Asim Riaz, Christin David, and Fiona J. Beck**

Complex 3D metallic nanostructures with large surface areas and broadband absorption are attractive candidates for efficient photocatalysis and spectroscopy. Here, hierarchical Au dendrites are self-assembled over centimeter-scales by electrodeposition and the plasmon modes are locally mapped using cathodoluminescence spectroscopy. A correlation between the spatial and spectral distribution of the plasmonic "hot-spots" and the morphology of these structures are demonstrated. Electrodynamic simulations show that the spectra of the plasmon modes are determined by the local geometry of sharp features. Their performance as both surface-enhanced Raman scattering (SERS) substrates and as photocatalysts for the *N*-demethylation reaction of methylene blue is investigated. High hot-spot densities result in larger SERS enhancement, while the sample with the lowest hot-spot density has a reaction yield 136% larger than the sample with the highest density. These findings indicate that maximizing the hot-spot density is not sufficient to optimize plasmonic substrates for all applications. The spectral and spatial distribution of the plasmon resonances will modify the hot electron generation efficiency and need to be considered for plasmon-enhanced photocatalysis. This work extends the understanding of light–matter interactions in complex 3D structures and provides direction for the rational design of plasmonic architectures for different applications.

1. Introduction

Nanostructured plasmonic materials provide unique opportunities for efficient and selective photocatalysis[1,2] and optical sensing,[3–5] thanks to their tailorable optoelectronic properties and excellent ability in interacting with adsorbed molecular species.[6] Plasmonic materials have the capacity to support localized resonances which strongly concentrate energy in subwavelength regions, often referred to as "hot-spots," where the local electric fields are significantly enhanced. Hot-spot regions play a fundamental role in surface enhanced Raman spectroscopy (SERS) and other molecular spectroscopies.[7]

Within the electromagnetic theory for SERS, the SERS intensity scales with the forth power of the local electric field intensity, thus substrates with high hot-spots density and strength are desirable,[8] while chemical enhancement could also affect the SERS performance.[9] The Raman signal of molecules within the hot-spots can be routinely amplified by a factor of $\approx 10^5$–10^6,[10] and plasmonic structures can be designed to achieve single molecule detection.[11] Hot-spots can also modify intrinsic physical and chemical properties of molecular adsorbates, promoting and enhancing chemical reactions by altering the surface potential energy landscape.[1,12,13]

Furthermore, these highly localized plasmonic resonances provide enhanced hot carrier generation from the nonradiative decay of the plasmon excitation, which can further boost the efficiency and selectivity of plasmon photocatalysis,[14] as recently demonstrated with hierarchical MoS2-based bimetallic structures.[15] Tailoring the energy distribution of these hot carriers can be achieved by appropriate choice of the plasmonic material, size, shape, and surrounding medium, and has been proven effective for solar applications including sensing, photodetectors and energy conversion.[16] Thus, the rational design and fabrication of plasmonic architectures featuring a multitude of intense and controllable hot-spots would be extremely beneficial for molecular detection and photocatalysis.

In the quest for hot-spot-rich devices, 2D disordered aggregates of metallic nanoparticles have shown significant local field enhancements with respect to their periodic counterparts,[17,18] with the additional advantage of relying on scalable,

Z. Fusco, A. Riaz, F. J. Beck
School of Engineering
College of Engineering and Computer Science
Australian National University
Acton, ACT 2601, Australia
E-mail: zelio.fusco@anu.edu.au; fiona.beck@anu.edu.au
C. David
Institute of Condensed Matter Theory and Optics
Friedrich-Schiller-Universität Jena
Max-Wien-Platz 1, 07743 Jena, Germany
C. David
Abbe Center of Photonics
Albert-Einstein-Straße 6, 07745 Jena, Germany

The ORCID identification number(s) for the author(s) of this article can be found under https://doi.org/10.1002/admi.202202236.

DOI: 10.1002/admi.202202236

bottom-up synthesis approaches.[18,19] These planar systems lead to efficient SERS substrates with single-molecule detection capability, whose high performances have been attributed to the multitude of strongly localized plasmonic resonances.[20] However, the energy and spatial distribution of the hot-spots do not correlate with the morphological properties, as experimentally demonstrated by spatially resolved electron-energy loss spectroscopy (EELS) measurements.[21] Understanding the spatial distribution of hot-spots is necessary to establish structure-performance relationships, which are important for the prescriptive design and optimization of plasmonic architectures toward tailored applications.[1]

Extending the highly localized plasmon-enhanced fields of disordered planar structures into 3D architectures is beneficial for applications that require increased surface area and larger plasmonic interaction volume.[4,22] For instance, it has been demonstrated that controllable 3D hierarchical structures are among the most efficient photoelectrocatalysts,[23–25] scatterers for SERS[11] and optical sensors,[4] as they enable novel optical phenomena,[26] strong field enhancement,[27] and higher generation of hot carriers.[24]

However, fabrication methods for large-scale 3D plasmonic structures which allow control of the spatial and spectral distribution of hot-spots are still elusive. Despite the superior control enabled by top-down lithographic techniques,[28] they are limited to sub-millimeter areas and maximum thicknesses of few hundreds of nanometers. Conversely, bottom-up techniques can realize 3D hierarchical stochastic structures over large-areas[25,26,29] featuring a multitude of hot-spots. In these systems, the stochastic arrangements of morphological features with multiple sizes, shapes, and connectivity enables excitation of multiple plasmon modes—demonstrating both highly localized hot-spots and collective effects[30]—ideal for plasmon-enhanced spectroscopy and photochemistry.[31] However, their limitation is a reduced spatial heterogeneity of the hot-spots, which can be largely ameliorated by averaging the measurements over large areas.[3]

Recently, 3D interconnected Ag networks were demonstrated to photo-reduce fullerene C60 due to the strongly confined nanoscale fields and enhanced hot electron generation and transfer.[25] The spatial and energy distribution of these hot-spots was further investigated by cathodoluminescence (CL) spectroscopy.[12] CL spectroscopy is an advanced electron microscopy technique that enables the investigation of optoelectronic properties of materials with nanometric spatial and spectral resolution.[32] It can provide similar information to EELS, with the advantage that CL does not require electron transmission through the sample.[33,34] Instead, CL spectroscopy uses an accelerated electron beam (1–50 keV) from scanning electron microscopes to excite all the available optical modes in a sample and measures energy distribution of the scattered photons, which is proportional to the local photon density of states (LDOS).[35] In a raster-scanning geometry, it is possible to retrieve the full spectrum from each pixel of the entire scanned sample with nanometer resolution. When CL was applied to the 3D interconnected Ag network, it was shown that those structures affected the LDOS due to their complex topology that supported a multitude of hot-spots whose eigenmodes show fluctuations in intensity and energy. However, a relationship between the hot-spot distribution and the topology was not observed.

In this work we map the spatial and spectral distribution of hot-spots in 3D complex Au structures, using high resolution CL spectroscopy. Hierarchical Au dendrites are deposited over centimeter-scale conductive substrates by a single-step electrodeposition technique, which allows statistical control of the morphology by modifying the electrodeposition time. We achieve complex Au structures with self-similar properties, high curvature regions, and multibranched architectures that result in broadband visible and near-infrared absorption. We show that they support a multitude of plasmon resonances in the wavelength range of 400–900 nm, which strongly correlate with the local morphology of the network. We demonstrate a controllable hot-spot density with the electrodeposition time, which increases by more than a threefold as the time increases from 100 to 400 s. Boundary element method (BEM) simulations on simplified geometries support the experimental results and show that the plasmon modes supported by the complex morphologies are determined by the details of the local geometry of sharp features. These results indicate that that the spatial and spectral distribution of hot-spots could be controlled by modifying the shape of the regions of high curvature in the structures, achievable for instance during the deposition phase. We then study their performance as SERS substrates for the detection of parts-per-million (ppm) concentration of methylene blue (MB) and as photocatalysts, by monitoring the *N*-demethylation reaction of MB. We show that a higher hot-spot density results in better SERS detection, while a lower hot-spot density leads to improved reaction yields. This work contributes to the understanding of light confinement in 3D disorder systems, by addressing the performance-morphology relationship and provides guidelines on how to design efficient plasmon-enhanced systems architectures for photocatalysis and detection.

2. Results and Discussion

A set of Au architectures with different morphologies were rapidly synthesized on conductive felt of stainless-steel fibers in a single electrodeposition step, at a constant applied cathodic current of 5 mA cm^{-2}. The morphologies were controlled by varying the deposition time from 100 to 400 s. This technique offers a wide range of control parameters—including solution specifications, temperature, voltage, and current values—and, being based on diffusion, has been used to self-assemble a variety of patterns, like dendrites, fractal, and porous structures.[36]

Figure 1a–d shows scanning electron microscopy (SEM) images of representative morphologies obtained under these conditions, along with the illustration of the observed structures (Figure 1e). The electrodeposition is initiated by a nucleation step followed by growth of the structures. For short deposition times (100 s), the sample morphology is characterized by spherical nanoparticles with diameters in the range of 35–50 nm, and porous irregular nanoclusters with sizes ranging from 200 to ≈1 µm.

When the time is increased to 200 s, new nucleation sites are continuously formed and gold atoms are deposited on the surface making it rougher. This results in an interconnected

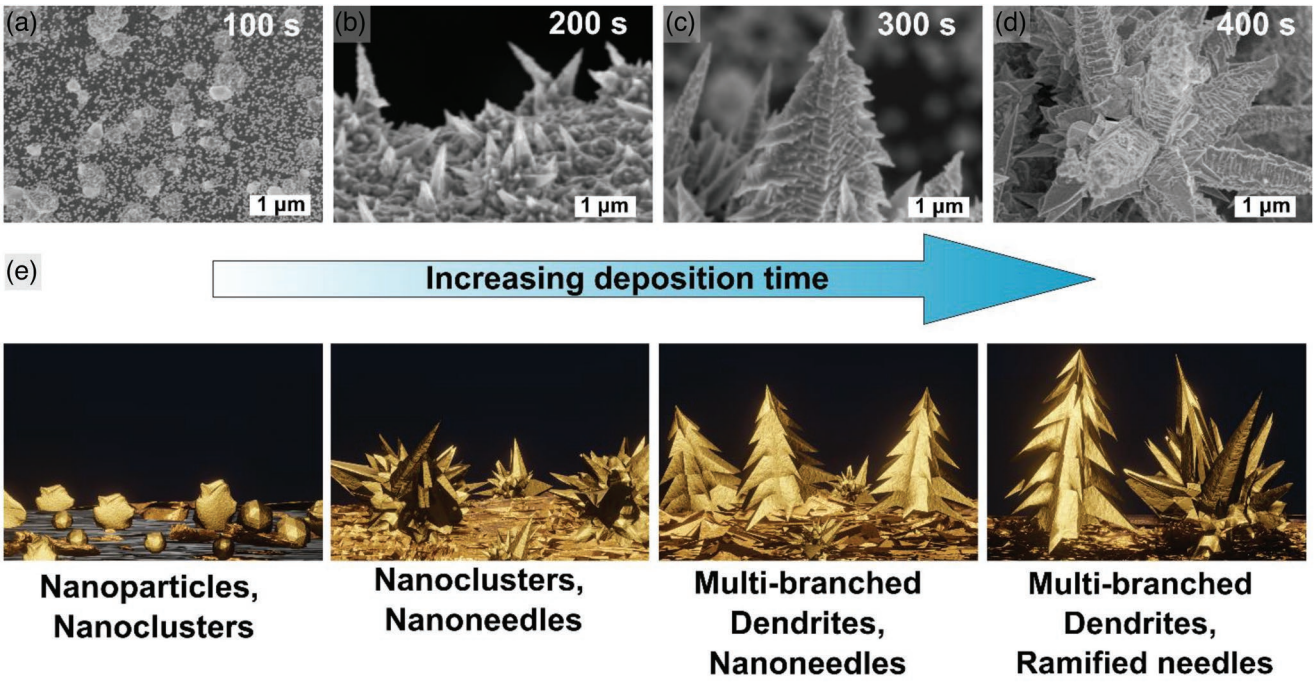

Figure 1. a–d) Representative SEM images of the Au nanostructures self-assembled with an applied current of 5 mA cm^{-2} at the different electrodeposition times of 100, 200, 300, and 400 s, respectively. e) Schematic evolution of structures with increasing deposition time.

metallic network consisting of nanoneedles and single-branched dendritic structures with tip radii ranging from ≈25 to ≈50 nm. The high surface roughness and the sharp tips lead to a strong nonuniform field that promotes the anisotropic deposition and development of branched morphology.[37] Further increase in the deposition time to 300 s leads to a morphological transition that drives the formation of self-similar 3D structures dominated by hierarchical and branched dendrites. The major axis of these ramified fractal architectures spans from ≈1–10 µm, while the length of the secondary orthogonal branches is in the range of 600 nm–1 µm. Importantly, these structures result in a high density of sharp tips, with diameters ranging from 20 to 60 nm. In the final investigated step of 400 s, this fractal morphology grows and becomes more compact, showing fractal dendrites and larger ramified structures, consistent with previous literature.[37]

This complex morphology leads to broadband absorption in the visible and near infrared (Figure S1, Supporting Information), which results from the average of the multiple plasmon modes excited on the complex structures.[12] To characterize the spatial and energy distribution of the resonances, we use spatially resolved CL spectroscopy. We start by acquiring panchromatic CL maps: the CL signal is integrated over all the wavelengths that fall within the detector range.[38] **Figure 2**a–d (and Figure S2, Supporting Information, for smaller magnification) shows the results of this measurements by overlaying the CL emission (blue spots) onto their respective SEM images (red), clearly demonstrating that the areas of strong CL signal correlate with morphological features of the structure, especially the sharp tips and edges. For 100 s electrodeposition time, we observe faint CL hot-spots arising predominantly from edges and surfaces of the NPs and nanoclusters, while for electrodeposition times ≥200 s, a strong emission due to excitation of plasmon modes is shown to follow the roughness and the high curvature regions of the architectures.

To estimate the density of hot-spots excited on the samples, we define a hot-spot as a region in which the CL emission has an intensity ≥50% of the total range and spanning at least 2 pixels, to avoid spikes and/or artifacts. A minimum of seven panchromatic maps covering a total surface area of at least 400 μm^2 were analyzed and then the results were averaged to obtain the averaged hot-spot density. This analysis reveals that the hot-spot density increases from $2.6 \pm 1.6\ \mu m^{-2}$ for the 100 s to $8.6 \pm 3.4\ \mu m^{-2}$ for the 400 s (Table S1, Supporting Information), indicating that the growth of the 3D dendritic structures is accompanied by a progressive increase of regions with strongly enhanced plasmon fields.

Here, we note that the results of this analysis are likely an underestimation. This is because the electron beam is impinging the samples orthogonally, probing the top of the samples. Any field enhancements that are obscured by features above them do not contribute to the calculation. This is particularly relevant for longer electrodeposition times because of the 3D branching of the architectures.

We further investigate the spectral distribution of the plasmon modes by analyzing CL emission for different samples in the wavelength range of 400–900 nm. We perform CL measurements in raster-scanning mode, which locally excites the nanostructure and then acquires a full spectrum for each pixel (minimum pixel size 0.013 × 0.013 µm) of the scanned image.

Figure 3a shows the panchromatic CL emission map from the 100 s sample with a typical nanoparticle morphology, overlaid with its SEM image. The CL signal shows homogeneous

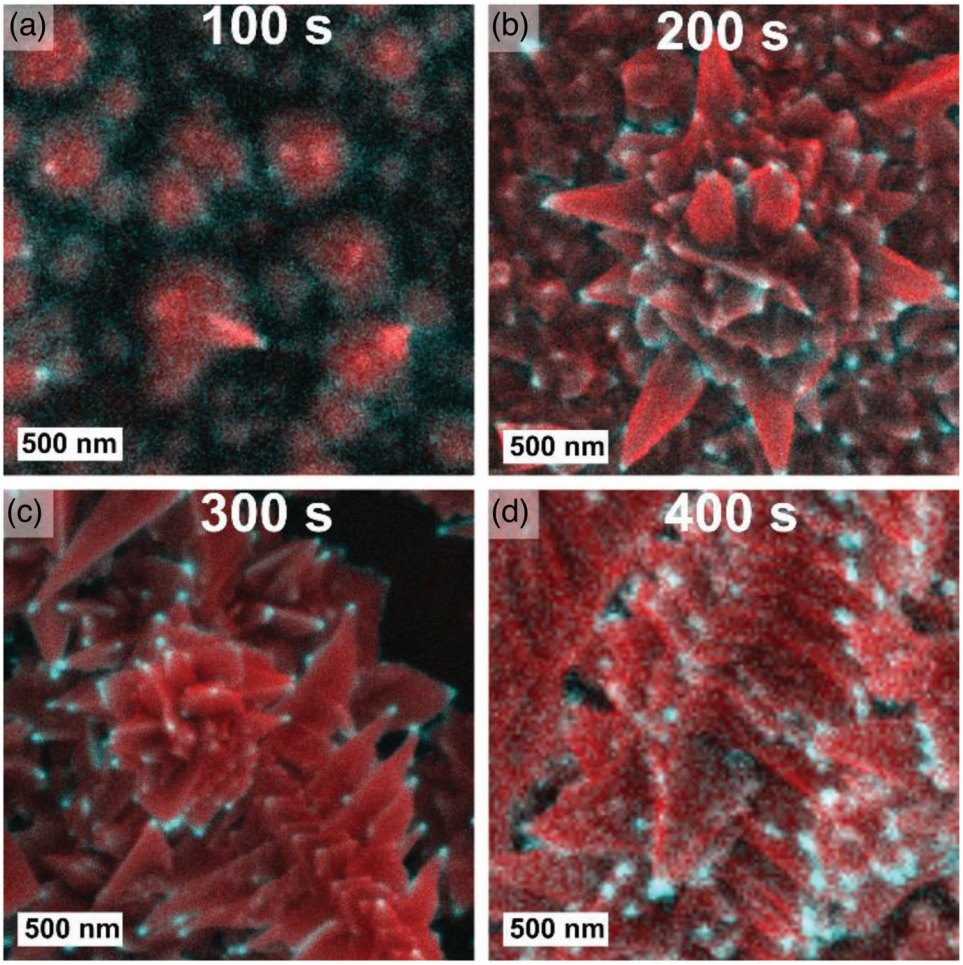

Figure 2. a–d) Superimposed panchromatic CL signal over the SEM images of the electrodeposited Au dendrites as a function of the electrodeposition times, from 100 to 400 s, respectively.

emission throughout the nanoparticles with stronger luminescence arising from the higher roughness regions and edges of the nanoparticles. Figure 3b–f shows the intensity maps obtained from the integration of the CL emission in different spectral ranges, characterized by $\lambda_{CL} = \lambda_i \pm 50$ nm, with $\lambda_i = 450$, 550, 650, 785, and 850 nm. These maps show a Mie-like CL signal with maximum strength in the wavelength range of 600–700 nm, consistent with spectral CL emission on disordered Au nanoparticles,[21,39] while the emission at wavelengths <500 and >800 nm is negligible (see Supporting Information S3 and S4 for further characterization). The CL spectra from different areas of the sample are highlighted in Figure 3g,h, corresponding to edges or high roughness regions (denoted as edge in g), and internal areas (denoted as bulk in h), as shown in Figure 3a. This analysis reveals, that the CL signal is always stronger for edges (positions 2, 3, and 4) and rough areas (positions 1 and 5) compared to the bulk while their maximum is observed always in the spectral region of 600–700 nm, in line with the Mie-like resonances of disconnected metal nanoparticles.[21]

Figure 4a (and Figure S5, Supporting Information) shows the panchromatic CL emission map from the 300 s sample—over an area corresponding to the secondary branching of a dendritic structure—overlaid with its SEM image. This measurement reveals strong CL emission localized at the sharp tips, confirming that the spatial distribution of the hot-spots is strongly correlated with the local structure. Following the same analysis as in Figure 3, Figure 4b–f shows the integrated CL maps in different spectral ranges, characterized by $\lambda_{CL} = \lambda_i \pm 50$ nm, with $\lambda_i = 450$, 550, 650, 750, and 850 nm. Similar to the previous case, the CL signal <500 nm is very faint (Figure 4b), indicating that below the intraband transition of gold (≈2.3 eV), there is no CL emission. Between 500 and 900 nm, the dendrites support hot-spots with marked spatial distribution comprised of different resonances, extending into the long wavelength region (Figure 4c–f).

For wavelengths of 500–600 nm a relatively uniform CL emission is observed throughout the whole branched architecture, with the appearance of hot-spots scattered mostly at the edges of the structure (see also Figure S5, Supporting Information). Between 600 and 700 nm, the emission is stronger and more concentrated at the tips and edges, while between 700 and 800 nm the CL emission from the broader structure becomes negligible, with strongly localized resonances occurring at the sharp tips. Beyond 800 nm the CL signal is much reduced, though still concentrated at the tips.

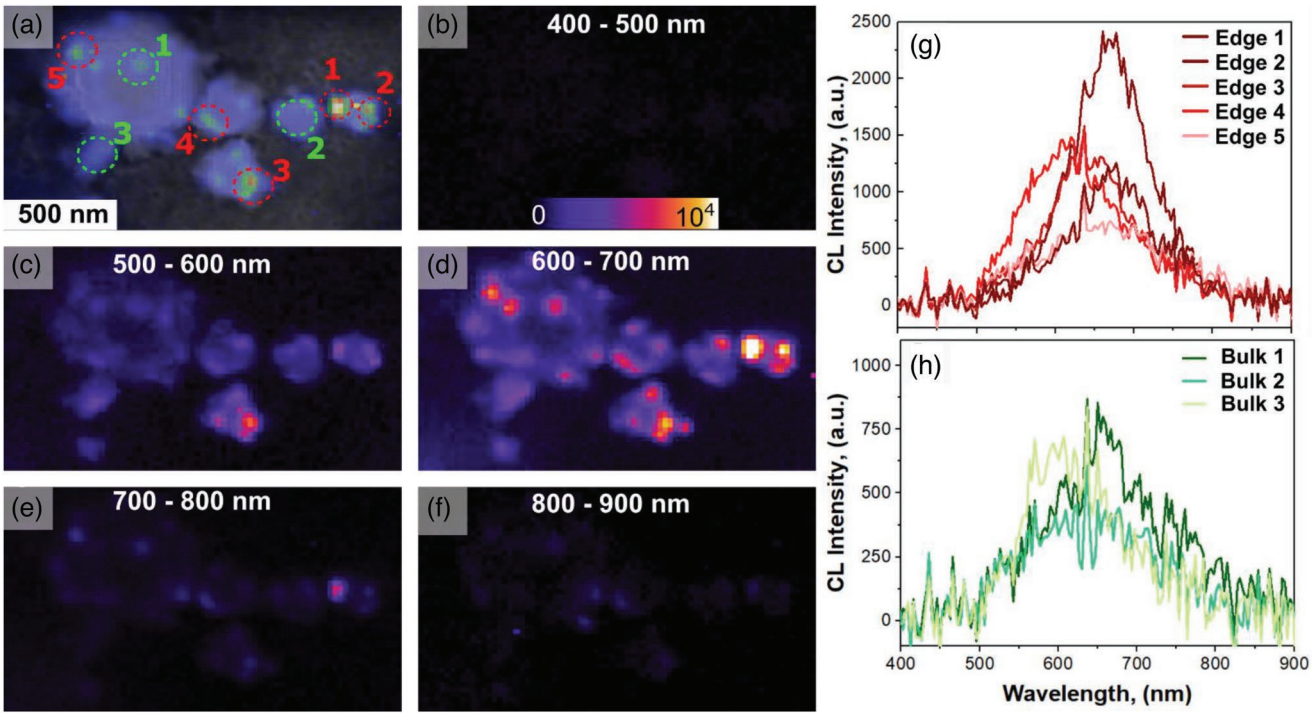

Figure 3. a) Panchromatic CL intensity map for the 100 s electrodeposited sample overlaid on the corresponding SEM image. b–f) CL intensity maps integrated over different wavelength ranges showing the excited modes. g,h) CL emission spectra at the positions indicated in panel (a), for g) the edges (red numbering) and h) bulk green numbering. All spectra represent an average taken over 2 × 2 neighboring pixels.

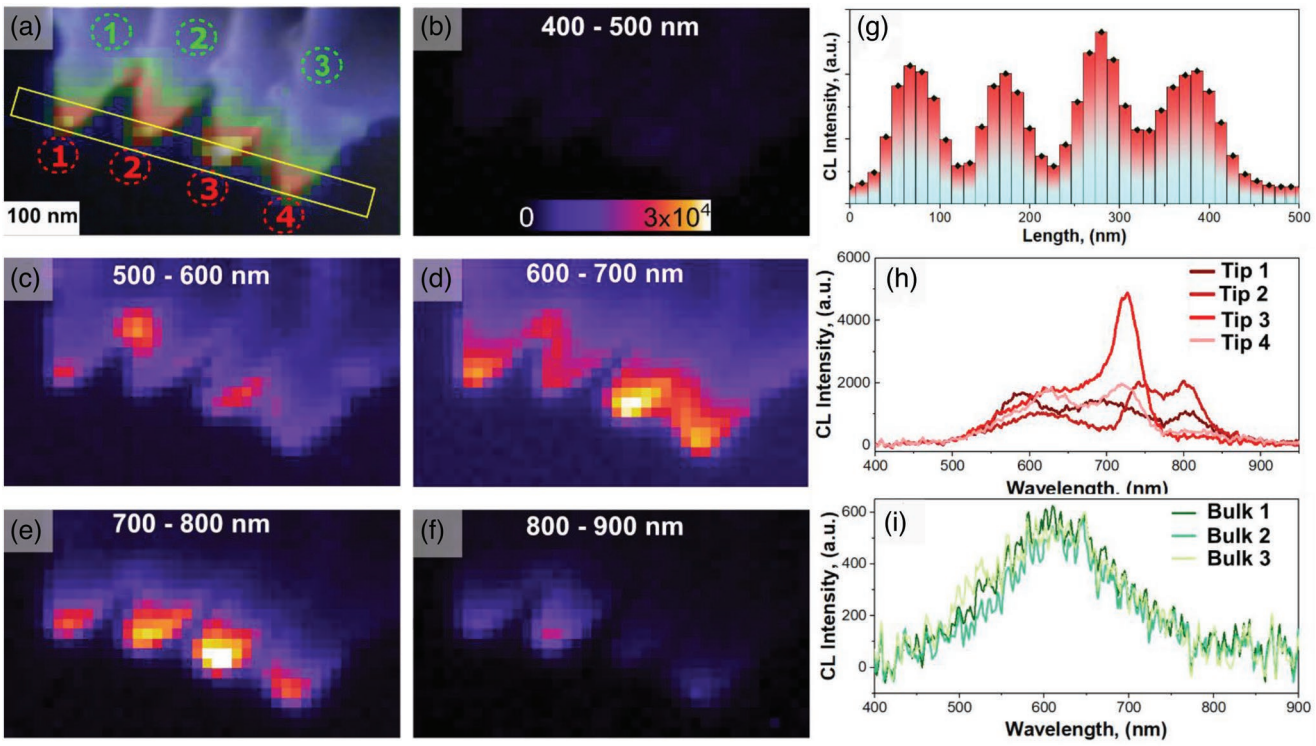

Figure 4. a) Panchromatic CL map of the 300 s sample showing strong localization at the structure tips. b–f) Intensity maps at different labeled wavelength ranges showing the excited modes in different spectral ranges. g) Line profile of the total/wavelength integrated/panchromatic CL signal of the region containing the dendrite tips, highlighted by the yellow box in panel (a). h,i) CL spectral emission from the tips and bulk, respectively, at the positions indicated respective color-coded numbering. All spectra represent an average taken over 2 × 2 neighboring pixels.

Figure 4g shows the total integrated panchromatic CL signal over the whole detector range in a region that includes the tips of the structure, highlighted by the yellow box in Figure 4a. This analysis further demonstrates the strong localization and spatial correlation of hot-spots at the tips with radii of curvature of ≈20 nm, showing a relatively uniform total CL emission, arising from the multiple resonances at different wavelengths.

The emission spectra of different points on the structure corresponding to the tips are given in Figure 4h, while the spectra from the internal part of the branches (bulk) are given in Figure 4i. The spectra of the tips span a broad wavelength region, ranging from 550–900 nm and are characterized by multiple resonances (peaks), with the strongest emerging at 720 nm from the tip #3. Interestingly, the spectral position of the strongest CL signals for all the investigated dendritic structures markedly varies between 600 and 800 nm (see also Figure S5, Supporting Information). Several other modes and shoulder peaks are also found outside this wavelength range suggesting possible coupling and hybridization between tips and core resonances,[34,40] which are likely to contribute to the broad absorption measured in the far field. The linewidth of these peaks, which is correlated to the radiative and resistive damping of the plasmon modes,[41] varies from ≈30 nm for the strongest resonances to ≈140 nm for broader peaks. In the internal regions farther from the peaks (bulk), we observe that the CL signal is an order of magnitude lower than at the tips, demonstrating a broad but relatively uniform emission peaked at ≈600 nm (Figure 4i), consistent with the CL of earlier work on unstructured Au surfaces.[42] Analysis of the 200 s sample shows similar results as shown in Figure S6, Supporting Information.

To better understand the optical behavior of our 3D dendritic structures and to further investigate the spectral distribution of the plasmon modes and their dependence on the local structure, we simulate the CL emission using the boundary element method[43] (BEM) implemented in the freely available MNPBEM toolbox.[44]

We postulate that since the CL emission is strongly localized at the tips of the branched dendritic structures, (as shown in Figure 4 and Figure S5, Supporting Information) the spectral behavior of the resonances will be dominated by the local geometry. Thus, we restrict the simulations to these regions, and approximate the tips as symmetrical cones and triangular prisms with different aspect ratios. Simulating the disordered Au structure in its entirety would be prohibitively computationally expensive and would not necessarily provide additional insights into the features that determine the spectral distribution of the hot-spots. Despite the much-simplified simulation geometry, this approach allows us to provide qualitative trends that are reflected by the experimental observations.

In **Figure 5**a,b, we plot the simulated CL emission intensity spectra of Au cones with widths (w) and heights (h) and we systematically vary those dimensions to investigate how the details of the local geometry determine the spectral dependence of emission at the tips of the dendritic structures. The results of this analysis show that the CL spectra of cones with a fixed width (50 nm) and varying heights (up to 300 nm) are characterized by multiple sharp peaks between 550 and 900 nm, which red-shift with the increase of the size. When the width is increased to 150 nm, the resonances are broader and still red-shift with the increase in height, and the shoulder resonances at ≈600 nm become more pronounced. Conversely, fixing the height at 100 nm and increasing the widths results in broader CL spectra with all the peaks blue-shifting as the size increases. Consistent with the experimental results, the field distribution follows the high curvature of the geometry and shows strongest localization at the tips of wider cones (Figure S7, Supporting Information). Similar results are obtained with Au triangular prisms (Figure 5c and Figure S8, Supporting Information). We find that keeping width (y) and height (z) constant at 150 and 50 nm, respectively and sweeping the length (x) from 200 to 350 nm red-shift and strengthen the main plasmonic peak between 700 and 850 nm. Conversely, increasing the width (y) results in sharper peaks between 700 and 750 nm that only slightly red-shift with the increasing size, and reduce in strength. Increasing the thickness of the triangular prisms (z) reduces and blue-shifts the main plasmonic peak. In all cases a shoulder peak emerges at lower wavelengths (≈550 nm).

The range and variation of the resonances observed in the simulations in Figure 5 are qualitatively similar to the experimentally measured CL spectra in Figure 4 and Figure S5, Sup-

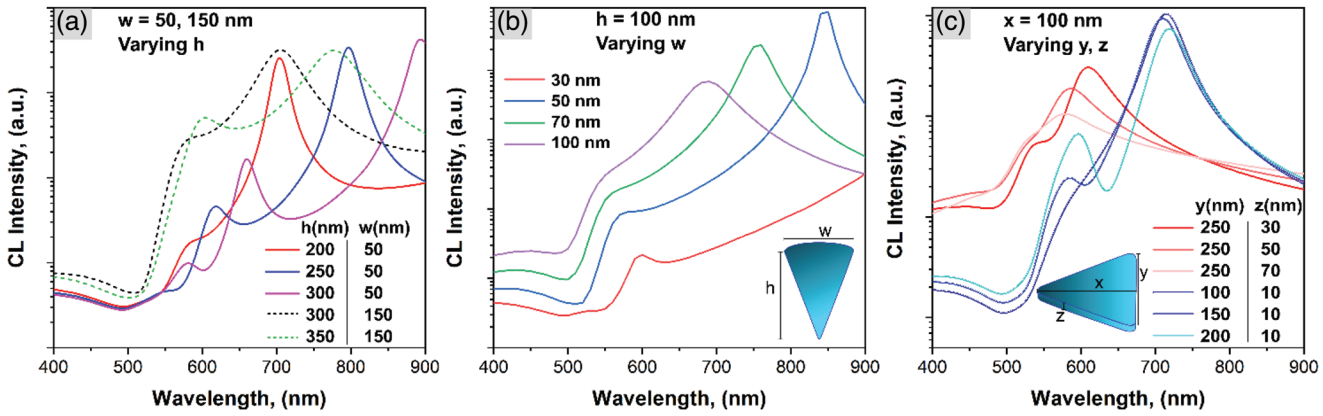

Figure 5. a,b) Numerically simulated cathodoluminescence spectra for Au cones with different aspect ratios, studied by systematically varying the height (h) and width (w), respectively. c) Cathodoluminescence spectra evaluated with the MNPBEM toolbox for Au triangular prisms with length fixed to 100 nm and different widths (y) and heights (z).

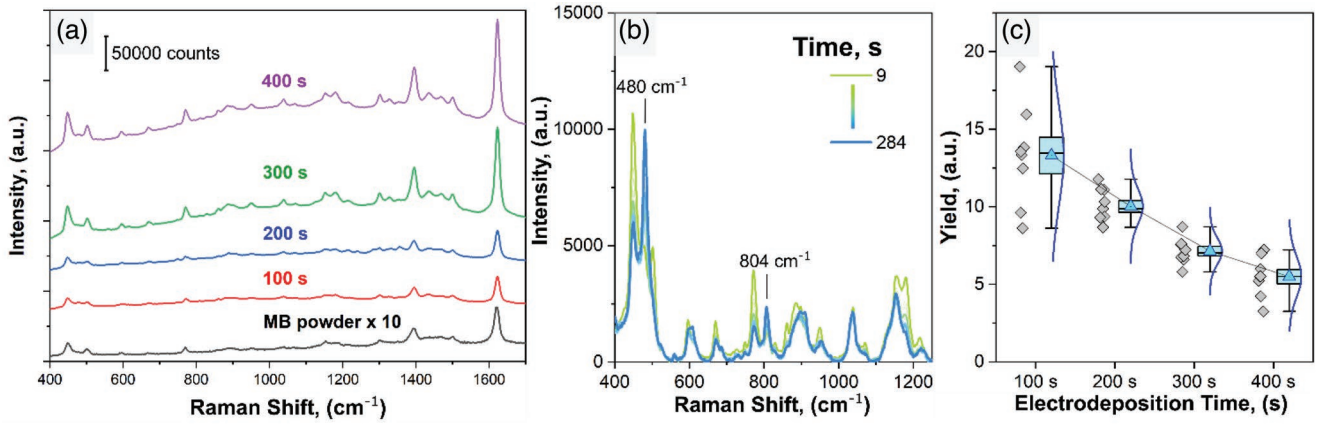

Figure 6. a) Stacked SERS spectra of 5 ppm MB on the different disordered Au substrates along with the spectra for MB powder (black line). b) In situ temporal evolution of the SERS spectra of MB adsorbed on a 100 s electrodeposited Au sample. c) Summary of the reaction yields as a function of the electrodeposition time. The grey diamonds show the distribution of individual and independent measurements, along with their Gaussian distribution (solid blue lines) and average yield (light blue triangles). The light grey line connects the average yield amongst the different samples.

porting Information. First, while the resonance peaks vary for different dimensions of the cones and triangular prisms, they all fall in the range of 500–900 nm, similar to the measured CL spectra in Figure 4. Second, the multiple peaks due to higher plasmon modes are well reproduced by the model. Third, the variations in the resonant wavelengths and intensities seen experimentally for different tips can be reproduced by changing the aspect ratio of the 3D geometries. Even though the simulated geometries are much simpler than the experimentally measured dendritic structures, this analysis demonstrates that 1) this simple model can qualitatively explain the multiple plasmonic modes observed in the Au structures; 2) the optical properties of the hot-spots are determined by the local geometry, rather than the overall interconnected sample morphology; and 3) there is a clear correlation between the tip shape and the spectral and spatial distribution of the plasmonic resonances and corresponding hot-spots.

Next, the performances of these disordered morphologies were investigated for two separate applications: SERS detection of 5 ppm solution of methylene blue (MB), and the plasmon-mediated photocatalytic reaction of MB. **Figure 6**a shows the Raman spectrum of MB powder (magnified ten times) along with the SERS spectra obtained from the disordered Au substrates with different electrodeposition times, functionalized overnight with a 5 ppm ethanol solution of MB and excited with λ_{exc} = 633 nm. The most intense peaks at 1622, 446, 1390, and 1426 cm^{-1} are assigned to the C—C ring stretching, skeletal deformation of C—N—C and C—N symmetric/asymmetric stretching, respectively.[45]

The more complex 3D Au substrates with 300 and 400 s electrodeposition time show a higher Raman signal intensity, than the 100 and 200 s case. This can be partially explained by the increasing hot-spot densities of the Au substrates with the electrodeposition time. However, as the SERS intensity is proportional to the number of molecules probed during the excitation it is also likely due to the larger illuminated surface area of the more complex 300 and 400 s samples.

The same samples were then used as photocatalysts for the photochemical reaction of MB to thionine, by monitoring the temporal evolution of the molecular fingerprints from in situ SERS measurements, illuminated by a 633 nm laser. We have previously shown that this reaction on disordered Au nanoparticle arrays[46] is maximized when the excitation wavelength matches the plasmonic resonance and the HOMO–LUMO gap (highest occupied molecular orbital–lowest unoccupied molecular orbital, which for MB is 1.86 eV = 665 nm[47]). Furthermore, we demonstrated that enhanced near-fields and hot electron transfer contribute synergistically to drive the chemical transformation, and that photothermal effects do not play a role.

Figure 6b shows the representative temporal evolution of the SERS spectra, taken over 284 s on the 100 s electrodeposited substrate. The SERS spectra show the emergence of peaks at 480 and 804 cm^{-1}, arising from the skeletal deformation mode and the NH_2 rocking vibration of thionine, respectively,[48] confirming the *N*-demethylation reaction that converts MB to thionine. To obtain the reaction yield, we followed our previously reported methodology:[46] each SERS spectrum in the temporal evolution was normalized to their maximum, and then the final timestep is deconvoluted in the range of 400–550 cm^{-1}, where the main product peak is observed (see Figure S9, Supporting Information, for details). Given that the intensity of any vibrational mode is proportional to the population of the excited molecules,[49] the yield of the photocatalytic reaction can then be obtained by integrating the thionine peak at 480 cm^{-1}, summarized in Figure 6c.

In order to ensure that the results were representative of the sample as a whole, and not dependent on the characteristics of one particular area of the complex morphology, we used a large illumination area of ≈8 µm and took multiple independent measurements (see Experimental Section). The results of each measurement are shown by the grey diamonds in Figure 5c, along with their Gaussian distribution (solid blue lines) and average yield (light blue triangles). We find that the reaction yield is also dependent on the electrodeposition time—and thus on the morphology and optical characteristics of the substrates. The average yield decreases from 13 ± 3 to 5.5 ± 1 as the electrodeposition time increases from 100 to 400 s, in contrast

to the SERS enhancement of the samples. This corresponds to more than a ≈136% increase in MB transformation for the 100 s deposition time compared to the 400 s sample. The higher fluctuations observed for the 100 s sample are attributed to the lower morphological homogeneity, which shows a combination of disconnected nanoparticles and nanoclusters. In all the other samples the distributions are much narrower indicating good reproducibility of the measurements.

The analysis of the experimental yields clearly indicates that hot-spot density is inversely correlated with performance as a photocatalyst for this set of samples. This is somewhat counter intuitive, as we would expect a larger number of hot-spots to lead to higher yield for a reaction that is driven by hot electrons and enhanced near fields,[46] both maximized at hot-spots. Photogenerated hot electrons contribute to the reaction by injection into hybridized metal-adsorbate states, while near fields efficiently pump energy into the molecular species. The efficiency of these competing/synergistic mechanisms depends on the plasmon energy, plasmon dephasing, and the interaction with the surrounding molecular species. Similar mechanisms have been investigated also in metal–semiconductor systems, where hot carriers, near-field and plasmon-induced resonant energy transfer can be opportunely optimized for solar energy harvesting.[50] These results suggest that high hot-spot densities are insufficient to optimize plasmonic substrates for photocatalysis and that the spectral and spatial distribution of plasmonic resonances is also important.

It has been shown that smaller nanoconfined metal structures have an increased probability of hot electron generation and injection efficiency, due to the reduced electron–electron and electron–phonon interactions[51] compared to larger structures. We postulate that the spatial distribution of the plasmon resonances on our complex structures will likely determine the efficiency of hot electrons generation: plasmonic resonances that are strongly localized on nanoscale features would experience more confinement and have hence higher hot electron generation efficiencies compared to plasmonic resonances excited over larger volumes.

The higher reaction yield observed for the samples with t = 100 s excited by a 633 nm laser is likely due to a combination of better spectral overlap of the resonances with the HOMO–LUMO gap of MB and higher hot electron generation efficiency in the small, confined nanoparticles compared to larger structures. The hot-spots excited on the nanoparticles and nanoclusters (t = 100 s) have resonances that fall in the range of 600–700 nm, and are very strongly localized to nanoscale features of the sample, as evidenced by the CL spectroscopy in Figure 3 and Figures S3 and S4, Supporting Information. In comparison, the resonances that occur on the larger dendritic structures (t = 400 s), occur at different wavelengths depending on the details of the local geometry, and those that fall between 600 and 700 nm are spread over features on the order of 100 nm (e.g., Figure 4 and Figure S5, Supporting Information).

The analysis above demonstrates the versatility of complex 3D Au architectures as both efficient SERS substrates and plasmon photocatalysts. Such disordered structures, supporting multiple plasmon modes, offer a scalable platform to enhance the vibrational modes of adsorbed molecular species and modify their potential energy landscape for energy redistribution. Those structures could be also engineered during the synthesis to achieve particular aspect ratios, preferential growth along a crystallographic phase or multibranched structures[52] to accessing specific reaction pathways and enable reaction selectivity.

3. Conclusions

In this work, we address the structure-performance relationship of 3D complex metallic structures, demonstrating that strong plasmon localization correlates with the local morphology of complex architectures. We use a scalable, single-step electrodeposition technique to self-assemble dendritic structures over centimeter-scale conductive substrates. By changing the electrodeposition time, we control the density of strongly localized plasmonic hot-spots, and we map their spatial and energy distribution with nanometric resolution. We find that multiple resonances across the visible and near infrared spectra are responsible for the broadband absorption. Further BEM simulations demonstrate that the spectral distribution of the plasmonic modes is determined by the local structure, providing insights into the role of the geometrical parameters to achieve strong light confinement and tailored resonances in different spectral regions. These structures are used as efficient 3D plasmonic substrates for molecular detection and transformation: we demonstrate that a higher hot-spot density results in optimal SERS performance but is not sufficient to optimize reaction yield when used for photocatalysis. Knowledge of the spectral and spatial distribution of the excited plasmonic modes suggests that localization of the hot-spots to smaller features (≈10 nm) could help improve hot electron generation efficiency, and hence reaction yield. These results can be leveraged to provide guidelines for the rational design of plasmonic architectures for tailored applications. Furthermore, this work extends the understanding on light–matter interactions in complex 3D structures, an area of both fundamental and practical interest for applications including spectroscopy and novel photonic devices.

4. Experimental Section

Sample Fabrication: Conductive and flexible stainless-steel felt substrates were sonicated in ethanol and water baths for 10 min to remove any contaminant. $HAuCl_4$ was dissolved in a 1 M HCl solution to obtain a metal concentration of 0.25 mM. The electrodeposition was carried out in a standard three-electrode configuration, using the stainless-steel as working electrode, Pt foil as counter electrode and Ag/AgCl as a reference electrode. The working electrode was immersed in the electrolyte solution and an applied constant cathodic current of 5 mA cm^{-2} was maintained for the duration of the experiments (100, 200, 300, and 400 s).

Characterization: A FEI Verios scanning electron microscope (SEM) operating at 3 kV and equipped with Everhart–Thornley and immersion in-lens detectors for secondary electrons detection, was used to image the morphology of the samples. The same system was used to acquire cathodoluminescence signals by using a Gatan MonoCL4 Elite system. Full spectrum CL maps were acquired using a charge-coupled device (CCD). The maps were acquiring at accelerating voltages of either 10 or 15 kV, depending on the quality of the signal and currents of 12 nA.

Absorption was calculated from total transmittance $T(\lambda)$ and reflectance $R(\lambda)$ spectra which were taken using a PerkinElmer Lambda 1050 UV–vis–NIR spectrometer equipped with an integrating sphere to collect both scattered and specular reflectance and transmittance from the surface of the sample. A PMT R6872 detector for the UV/vis wavelength range and a Peltier-cooled InGaAs detector covering the 860–1800 nm range. Numerical simulations of the CL response were performed using the graphic interface (MNPBEM-GUI from Nikolaos Matthaiakakis of the MNPBEM toolbox.[44] Their optical properties were taken from the Johnson and Christy tabulated data,[53] while an electron beam excitation that mimics the experimental conditions was set, having an energy of 15 keV and a finite width of 1 nm, impinging orthogonally at the tip of the Au triangle. SERS measurements of methylene blue (from Sigma-Aldrich) were carried out using a Renishaw InVia Reflex spectrometer equipped with a 633 nm laser at a power of 0.33 mW and a 1200 l mm^{-1} grating. The samples were immersed overnight in a 5 ppm MB solution in ethanol, and gently rinsed with water before and let dry naturally before starting the SERS measurements. All the SERS measurements were performed at room-temperature in standard atmosphere with an acquisition time of 1 s and two accumulations for noise reduction. The SERS measurements were acquired with a 5× objective producing a spot size of ≈8 µm.

Supporting Information

Supporting Information is available from the Wiley Online Library or from the author.

Acknowledgements

The authors acknowledge the financial support by the Australian Reasearch Council (ARC). F.J.B. gratefully acknowledges the support of the ARC DECRA Fellowship (DE180100383) and META-ACTIVE—International Research Training Group (IRTG 2675). All the authors the authors acknowledge the use of the Australian National Fabrication Facility (ANFF), ACT Node.

Conflict of Interest

The authors declare no conflict of interest.

Data Availability Statement

The data that support the findings of this study are available from the corresponding author upon reasonable request.

Keywords

3D plasmonics, cathodoluminescence, hot electrons, multiscale optical systems, photocatalysis

Received: October 18, 2022
Revised: November 11, 2022
Published online:

[1] A. G. M. da Silva, T. S. Rodrigues, J. Wang, P. H. C. Camargo, *Chem. Commun.* **2022**, *58*, 2055.
[2] a) D. F. Swearer, H. Zhao, L. Zhou, C. Zhang, H. Robatjazi, J. M. Martirez, C. M. Krauter, S. Yazdi, M. J. McClain, E. Ringe, E. A. Carter, P. Nordlander, N. J. Halas, *Proc. Natl. Acad. Sci. U. S. A.* **2016**, *113*, 8916; b) L. Mascaretti, A. Dutta, S. Kment, V. M. Shalaev, A. Boltasseva, R. Zboril, A. Naldoni, *Adv. Mater.* **2019**, *31*, 1805513; c) Z. Zhang, C. Zhang, H. Zheng, H. Xu, *Acc. Chem. Res.* **2019**, *52*, 2506.
[3] A. Balčytis, Y. Nishijima, S. Krishnamoorthy, A. Kuchmizhak, P. R. Stoddart, R. Petruškevičius, S. Juodkazis, *Adv. Opt. Mater.* **2018**, *6*, 1800292.
[4] Z. Fusco, M. Rahmani, T. Tran-Phu, C. Ricci, A. Kiy, P. Kluth, E. Della Gaspera, N. Motta, D. Neshev, A. Tricoli, *Adv. Mater.* **2020**, *32*, 2002471.
[5] a) Z. Fusco, M. Rahmani, R. Bo, R. Verre, N. Motta, M. Käll, D. Neshev, A. Tricoli, *Adv. Mater.* **2018**, *30*, 1800931; b) M. Li, S. K. Cushing, N. Wu, *Analyst* **2015**, *140*, 386.
[6] a) V. N. Pustovit, T. V. Shahbazyan, *Phys. Rev. B* **2011**, *83*, 085427; b) A. Salomon, C. Genet, T. W. Ebbesen, *Angew. Chem., Int. Ed.* **2009**, *48*, 8748.
[7] a) J. Szczerbiński, L. Gyr, J. Kaeslin, R. Zenobi, *Nano Lett.* **2018**, *18*, 6740; b) F. Neubrech, C. Huck, K. Weber, A. Pucci, H. Giessen, *Chem. Rev.* **2017**, *117*, 5110.
[8] a) M. S. S. Bharati, V. R. Soma, **2010**, *4*, 210048; b) L. Hou, M. Shao, Z. Li, X. Zhao, A. Liu, C. Zhang, X. Xiu, J. Yu, Z. Li, *Opt. Express* **2020**, *28*, 29357; c) C. Zhang, C. Ji, J. Yu, Z. Li, Z. Li, C. Li, S. Xu, W. Li, B. Man, X. Zhao, *Opt. Express* **2021**, *29*, 38768.
[9] a) C. Ji, J. Lu, B. Shan, F. Li, X. Zhao, J. Yu, S. Xu, B. Man, C. Zhang, Z. Li, *J. Phys. Chem. Lett.* **2022**, *13*, 8864; b) I. H. Öner, C. David, C. J. Querebillo, I. M. Weidinger, K. H. Ly, *Sensors* **2022**, *22*, 487; c) I. H. Öner, C. J. Querebillo, C. David, U. Gernert, C. Walter, M. Driess, S. Leimkühler, K. H. Ly, I. M. Weidinger, *Angew. Chem., Int. Ed.* **2018**, *57*, 7225.
[10] J. Langer, D. Jimenez de Aberasturi, J. Aizpurua, R. A. Alvarez-Puebla, B. Auguié, J. J. Baumberg, G. C. Bazan, S. E. J. Bell, A. Boisen, A. G. Brolo, J. Choo, D. Cialla-May, V. Deckert, L. Fabris, K. Faulds, F. J. García de Abajo, R. Goodacre, D. Graham, A. J. Haes, C. L. Haynes, C. Huck, T. Itoh, M. Käll, J. Kneipp, N. A. Kotov, H. Kuang, E. C. Le Ru, H. K. Lee, J.-F. Li, X. Y. Ling, et al., *ACS Nano* **2020**, *14*, 28.
[11] P. Mao, C. Liu, G. Favraud, Q. Chen, M. Han, A. Fratalocchi, S. Zhang, *Nat. Commun.* **2018**, *9*, 5428.
[12] R. Ron, M. S. Zielinski, A. Salomon, *Nano Lett.* **2020**, *20*, 8205.
[13] a) D. Liu, C. Xue, *Adv. Mater.* **2021**, *33*, 2005738; b) C. Climent, J. Galego, F. J. Garcia-Vidal, J. Feist, *Angew. Chem., Int. Ed.* **2019**, *58*, 8698.
[14] a) A. Sousa-Castillo, M. Comesaña-Hermo, B. Rodríguez-González, M. Pérez-Lorenzo, Z. Wang, X.-T. Kong, A. O. Govorov, M. A. Correa-Duarte, *J. Phys. Chem. C* **2016**, *120*, 11690; b) P. Christopher, H. Xin, A. Marimuthu, S. Linic, *Nat. Mater.* **2012**, *11*, 1044; c) L. Mascaretti, A. Naldoni, *J. Appl. Phys.* **2020**, *128*, 041101.
[15] C. Zhang, Z. Li, S. Qiu, W. Lu, M. Shao, C. Ji, G. Wang, X. Zhao, J. Yu, Z. Li, *Nanophotonics* **2022**, *11*, 33.
[16] H. Tang, C.-J. Chen, Z. Huang, J. Bright, G. Meng, R.-S. Liu, N. Wu, *J. Chem. Phys.* **2020**, *152*, 220901.
[17] a) K. Kneipp, H. Kneipp, I. Itzkan, R. R. Dasari, M. S. Feld, *Chem. Rev.* **1999**, *99*, 2957; b) K. Li, M. I. Stockman, D. J. Bergman, *Phys. Rev. Lett.* **2003**, *91*, 227402.
[18] Z. Fusco, R. Bo, Y. Wang, N. Motta, H. Chen, A. Tricoli, *J. Mater. Chem. C* **2019**, *7*, 6308.
[19] a) J. Wu, X. Zhou, P. Li, X. Lin, J. Wang, Z. Hu, P. Zhang, D. Chen, H. Cai, R. Niessner, C. Haisch, P. Sun, Y. Zheng, Z. Jiang, H. Zhou, *Anal. Chem.* **2021**, *93*, 8799; b) L. Fabris, *Chem. Commun.* **2012**, *48*, 9346.
[20] a) M. Stockman, *Physics* **2010**, 3; b) M. I. Stockman, V. M. Shalaev, M. Moskovits, R. Botet, T. F. George, *Phys. Rev. B* **1992**, *46*, 2821.

[21] A. Losquin, S. Camelio, D. Rossouw, M. Besbes, F. Pailloux, D. Babonneau, G. A. Botton, J.-J. Greffet, O. Stéphan, M. Kociak, *Phys. Rev. B* **2013**, *88*, 115427.
[22] J. J. Mock, R. T. Hill, Y.-J. Tsai, A. Chilkoti, D. R. Smith, *Nano Lett.* **2012**, *12*, 1757.
[23] S. C. Warren, K. Voitchovsky, H. Dotan, C. M. Leroy, M. Cornuz, F. Stellacci, C. Hebert, A. Rothschild, M. Gratzel, *Nat. Mater.* **2013**, *12*, 842.
[24] M. Graf, D. Jalas, J. Weissmüller, A. Y. Petrov, M. Eich, *ACS Catal.* **2019**, *9*, 3366.
[25] R. Ron, D. Gachet, K. Rechav, A. Salomon, *Adv. Mater.* **2017**, *29*, 1604018.
[26] Y. Tian, F. P. Garcia de Arquer, C. T. Dinh, G. Favraud, M. Bonifazi, J. Li, M. Liu, X. Zhang, X. Zheng, M. G. Kibria, S. Hoogland, D. Sinton, E. H. Sargent, A. Fratalocchi, *Adv. Mater.* **2017**, *29*, 1701165.
[27] M. Liu, Y. Pang, B. Zhang, P. De Luna, O. Voznyy, J. Xu, X. Zheng, C. T. Dinh, F. Fan, C. Cao, F. P. G. de Arquer, T. S. Safaei, A. Mepham, A. Klinkova, E. Kumacheva, T. Filleter, D. Sinton, S. O. Kelley, E. H. Sargent, *Nature* **2016**, *537*, 382.
[28] a) C. M. Soukoulis, M. Wegener, *Nat. Photonics* **2011**, *5*, 523; b) G. Yoon, I. Kim, S. So, J. Mun, M. Kim, J. Rho, *Sci. Rep.* **2017**, *7*, 6668.
[29] a) J. Erlebacher, M. J. Aziz, A. Karma, N. Dimitrov, K. Sieradzki, *Nature* **2001**, *410*, 450; b) N. Takeyasu, N. Taguchi, N. Nishimura, B. H. Cheng, S. Kawata, *APL Photonics* **2016**, *1*, 050801.
[30] R. Ron, E. Haleva, A. Salomon, *Adv. Mater.* **2018**, *30*, 1706755.
[31] a) F. Su, T. Wang, R. Lv, J. Zhang, P. Zhang, J. Lu, J. Gong, *Nanoscale* **2013**, *5*, 9001; b) M.-H. Shiao, T. Wu, H. J. Huang, C.-Y. Peng, Y.-S. Lin, T.-Y. Lai, Y.-W. Lin, *Nanomaterials* **2021**, *11*, 1359.
[32] a) A. Polman, M. Kociak, F. J. García de Abajo, *Nat. Mater.* **2019**, *18*, 1158; b) M. Bosman, G. R. Anstis, V. J. Keast, J. D. Clarke, M. B. Cortie, *ACS Nano* **2012**, *6*, 319; c) T. Coenen, N. M. Haegel, *Appl. Phys. Rev.* **2017**, *4*, 031103.
[33] a) A. L. Koh, K. Bao, I. Khan, W. E. Smith, G. Kothleitner, P. Nordlander, S. A. Maier, D. W. McComb, *ACS Nano* **2009**, *3*, 3015; b) Z. Fusco, M. Taheri, R. Bo, T. Tran-Phu, H. Chen, X. Guo, Y. Zhu, T. Tsuzuki, T. P. White, A. Tricoli, *Nano Lett.* **2020**, *20*, 3970.
[34] M. Liebtrau, M. Sivis, A. Feist, H. Lourenço-Martins, N. Pazos-Pérez, R. A. Alvarez-Puebla, F. J. G. de Abajo, A. Polman, C. Ropers, *Light: Sci. Appl.* **2021**, *10*, 82.
[35] F. J. García de Abajo, *Rev. Mod. Phys.* **2010**, *82*, 209.
[36] a) A. Bunde, S. Havlin, *Fractals and Disordered Systems*, 2nd ed., Springer, New York **1996**; b) A. Kumar, J. M. Gonçalves, A. Sukeri, K. Araki, M. Bertotti, *Sens. Actuators, B* **2018**, *263*, 237.
[37] R. Yu, J. Wang, M. Han, M. Zhang, P. Zeng, W. Dang, J. Liu, Z. Yang, J. Hu, Z. Tian, *ACS Omega* **2020**, *5*, 8293.
[38] G. Salviati, *Scanning* **1993**, *15*, 350.
[39] Z. Fusco, M. Rahmani, R. Bo, T. Tran-Phu, M. Lockrey, N. Motta, D. Neshev, A. Tricoli, *Adv. Funct. Mater.* **2019**, *29*, 1806387.
[40] A. C. Y. Liu, J. Lloyd, T. Coenen, D. E. Gómez, *Microsc. Microanal.* **2020**, *26*, 808.
[41] T. Coenen, B. J. M. Brenny, E. J. Vesseur, A. Polman, *MRS Bull.* **2015**, *40*, 359.
[42] X. Ma, M. Grüßer, R. Schuster, *J. Phys. Chem. C* **2014**, *118*, 23247.
[43] a) F. J. García de Abajo, A. Howie, *Phys. Rev. B* **2002**, *65*, 115418; b) F. J. García de Abajo, A. Howie, *Phys. Rev. Lett.* **1998**, *80*, 5180.
[44] U. Hohenester, A. Trügler, *Comput. Phys. Commun.* **2012**, *183*, 370.
[45] a) G.-N. Xiao, S.-Q. Man, *Chem. Phys. Lett.* **2007**, *447*, 305; b) R. R. Naujok, R. V. Duevel, R. M. Corn, *Langmuir* **1993**, *9*, 1771.
[46] Z. Fusco, K. Catchpole, F. J. Beck, *J. Mater. Chem. C* **2022**, *10*, 7511.
[47] O. V. Ovchinnikov, A. V. Evtukhova, T. S. Kondratenko, M. S. Smirnov, V. Y. Khokhlov, O. V. Erina, *Vib. Spectrosc.* **2016**, *86*, 181.
[48] T. E. Tesema, B. Kafle, M. G. Tadesse, T. G. Habteyes, *J. Phys. Chem. C* **2017**, *121*, 7421.
[49] R. C. Maher, C. M. Galloway, E. C. Le Ru, L. F. Cohen, P. G. Etchegoin, *Chem. Soc. Rev.* **2008**, *37*, 965.
[50] S. K. Cushing, A. D. Bristow, N. Wu, *Phys. Chem. Chem. Phys.* **2015**, *17*, 30013.
[51] a) H.-H. Shin, J.-J. Koo, K. S. Lee, Z. H. Kim, *Appl. Mater. Today* **2019**, *16*, 112; b) A. O. Govorov, H. Zhang, Y. K. Gun'ko, *J. Phys. Chem. C* **2013**, *117*, 16616; c) R. Sundararaman, P. Narang, A. S. Jermyn, W. A. GoddardIII, H. A. Atwater, *Nat. Commun.* **2014**, *5*, 5788.
[52] a) P. Sebastián-Pascual, I. Jordão Pereira, M. Escudero-Escribano, *Chem. Commun.* **2020**, *56*, 13261; b) T.-H. Lin, C.-W. Lin, H.-H. Liu, J.-T. Sheu, W.-H. Hung, *Chem. Commun.* **2011**, *47*, 2044.
[53] P. B. Johnson, R. W. Christy, *Phys. Rev. B* **1972**, *6*, 4370.